Electrical characterization of coupled and uncoupled MEMS ultrasonic transducers

I.J. Oppenheim, A. Jain, and D.W. Greve, *Member, IEEE*

***Abstract*—We report electrical characterization of micromachined polysilicon capacitive diaphragms for use as ultrasonic transducers. Admittance measurements yield insight into the resonant behavior and also the damping resulting from ultrasonic radiation and frictional forces due to the etch release holes. Unbonded transducers exhibit sharp resonances with Q values that increase with decreasing air pressure. We also report for the first time direct bonding of these transducers to solid surfaces. Transducers survive the bonding process and show distinctly different displacement in response to applied DC bias. Finally, a single-degree-of-freedom model is used to obtain insight into the various contributions to damping.**

***Index Terms*—capacitive diaphragm, micromachined, transducer, ultrasonic**

I. Introduction

MICROMACHINED ultrasonic transducers have been recently investigated for a number of applications. A major attraction of these transducers is the possibility of fabricating transducer arrays that can be applied to imaging and phased-array detection. However, MEMS ultrasonic transducers differ in important ways from well-established piezoelectric transducers. These include a very great difference in the transducer acoustic impedance that leads to vastly different coupling behavior. In addition, the comparative fragility of MEMS transducers makes it challenging to devise ways to use them coupled to solids.

In this paper, we explore the electrical behavior of capacitive diaphragm transducers that are coupled to either air or solids. Our focus is on understanding and modeling the coupling between the electrical and mechanical domains. Prior published work has generally concerned transducers coupled to air or fluids [1,2,3,4]. Other work has also demonstrated the potential applications of these fluid-coupled transducers in imaging arrays [5,6] and non-destructive testing [7]. This paper reports for the first time characterization of MEMS transducers directly coupled to solids, that in principle can yield greatly increased sensitivity compared to air-coupled transducers. We also develop a single-degree-of-freedom (SDOF) model for the diaphragm that is used elsewhere to understand coupling of acoustic energy from a solid into the transducer.

Specifically, we study a polysilicon diaphragm transducer fabricated using the multi-user MUMPS process. This

work supplements other published work that focused on transducers intended for fluid coupling fabricated in a variety of custom processes. Elsewhere, we will report initial results on the application of these devices to ultrasonic testing of solid materials [8].

II. THEORY: DIAPHRAGM ADMITTANCE

We briefly present a lumped-element or single degree of freedom (SDOF) model. Some elements of the discussion follow a publication by Ladabaum et al. [9]. We model the diaphragm by a SDOF piston with a mass *m*, spring constant *k*, and dashpot constant c. The equation of motion for the piston deflection *x(t)* is

$$m\frac{d^2x}{dt^2} = -kx - c\frac{dx}{dt} + \frac{\varepsilon_0 S V^2(t)}{2(g-x)^2} + P(t)S \tag{1}$$

where *S* is the area of the piston as well as the overlap area between top and bottom electrodes, *g* is the gap between electrodes in the undeflected state, and *P(t)* is the pressure due to an ultrasonic wave. With a DC applied voltage and no ultrasonic wave we have a static displacement *x*

$$x \approx \frac{\varepsilon_0 S V_{DC}^2}{2kg^2} \tag{2}$$

and consequently the capacitance *C* measured using a frequency far from piston resonance is given by

$$C(V) = \frac{\varepsilon_0 S}{g}\left(1 + \frac{\varepsilon_0 S V^2}{2kg^3}\right) = C_0 + C_1 V^2 \tag{3}$$

When near resonance, vibration of the piston must be considered and we write $V(t) = V_{DC} + V_{ac}e^{j\omega t}$; keeping only linear terms the displacement *x(t)* becomes

$$x(t) = \mathrm{Re}\left[\frac{\varepsilon_0 S}{g^2}\frac{V_{DC}V_{ac}e^{j\omega t}}{k - m\omega^2 + j\omega c}\right]. \tag{4}$$

The current into the capacitor terminals is

$$i(t) = C\frac{dV}{dt} + V\frac{dC}{dt} = C\frac{dV}{dt} + V\frac{\varepsilon_0 S}{g^2}\frac{dx}{dt} \tag{5}$$

thus

$$i(t) = \mathrm{Re}\left[j\omega C_0 V_{ac}e^{j\omega t}\right] + n\frac{dx}{dt} \tag{6}$$

where $n = V_{DC}\varepsilon_0 S/g^2$. The electrical admittance is then

$$Y = j\omega C_0 + n^2 \frac{j\omega}{k - m\omega^2 + j\omega b} = j\omega C_0 + \frac{V_{DC}{}^2 C_0{}^2}{mg^2} \frac{j\omega}{\omega_0{}^2 - \omega^2 + j\omega\omega_0 / Q} \tag{7}$$

where $\omega_0 = (k/m)^{1/2}$. Q here represents the mechanical Q in the sense of Blitz [10] rather than the electrical Q derived by Ladabaum et al. [1]. The Q is influenced by a number of factors, including internal friction of the polysilicon diaphragm, radiation of acoustic energy, and squeeze film damping due to air flowing through the etch holes. When the primary loss mechanism is radiation of ultrasonic energy, it can be shown that $Q = (mk)^{1/2}/Z_{medium}S$, where Z_{medium} is the acoustic impedance of the medium coupled to the transducer.

III. Device fabrication

Figure 1a shows a cross section and top view of one capacitive diaphragm. The structure shown was fabricated in the multi-user MUMPS process [11]. Multi-user processes provide for convenient and economical fabrication of microelectronic prototypes although there are important limitations as it is not possible for the designer to influence the process parameters. In the case of the MUMPS process, the gap between upper and lower polysilicon electrodes is fixed at 2.0 microns and the upper polysilicon electrode thickness is 2.0 micron. The diaphragm was designed for a resonant frequency near 5 MHz. There is a residual film stress in the upper polysilicon layer, denoted σ, that is equal to -10 (± 10) MPa; the residual stress will be shown to have a negligible effect on the diaphragm resonant frequency. Holes 5 microns square are placed approximately 30 microns apart to provide for etching and release of the diaphragm. Devices were released at CRONOS using wet etching followed by supercritical drying. Supercritical drying displaces the release etch rinse water first by methanol and then by supercritical CO_2. When supercritical CO_2 is removed no gas-to-liquid phase boundary is formed and consequently layers are not pulled together by capillary forces. Subsequently, back contacts were provided by etching the back surface of the wafer with concentrated HF followed by deposition of aluminum.

It needs to be noted that this structure is somewhat non-optimal in that the parasitic capacitances to ground are rather large. In addition, the design does not take advantage of the DIMPLE mask level that is available in the MUMPS process [11] to reduce the spacing between the diaphragm electrodes. However, this structure does have the advantage of mechanical simplicity that makes it possible to apply structural formulae with some confidence.

As the capacitance of a single diaphragm is quite small, arrays of 180 diaphragms were connected in parallel to make a single transducer. The test chip included an array of nine identical transducers arranged along a line, in addition to other structures not discussed here. A mask layout of one transducer is shown in Fig. 1b. Cross sections

showing several steps in the process are presented in Fig. 2.

IV. Experimental Results

Electrical characterization was performed using an HP 4280A 1 MHz capacitance meter and an HP 4192A impedance analyzer. The HP 4280A can supply bias voltages up to 100 V and was used to verify detector operation by direct measurement of the diaphragm deflection. These measurements were performed using a 30 mV probe voltage. The HP 4192A was used to perform admittance-voltage measurements over the 100 kHz- 6 MHz frequency range; in these measurements the probe voltage was set to 1 V.

Some measurements were performed on transducers wirebonded in a ceramic package with air pressures ranging from coarse vacuum up to 1 atmosphere. Other transducers were acoustically coupled to a plexiglas prism using Gelest Zipcone CG silicone adhesive [12], that was brush-applied to the plexiglas followed by chip placement. The resulting silicone layer was about 0.25 mm in thickness. Visual inspection showed a few small bubbles (~ 50 μm diameter) for each transducer representing in all cases less than 5% of the transducer area. These transducers were contacted using a standard probe station.

A. Uncoupled Transducers

Figure 3 shows *C(V)* measurements performed on an uncoupled device. Figure 3 also shows a best-fit line to the data points illustrating excellent agreement with eq. (3) and yielding the value $C_1 = 1.71 \times 10^{-18}$ F/V^2.

C_0 can be predicted from the total overlap area of the top and bottom plates and the gap dimension. We predict $C_0 = 2.91 \times 10^{-12}$ F which is smaller than the measured capacitance at $V_{DC} = 0$. This is due to various parasitic capacitances associated with our non-optimized structure. Parallel stray capacitance arises from the stray capacitance to the substrate at each of the transducer terminals in conjunction with the substrate contact resistance. These parasitic capacitances are independent of bias voltage and have weak frequency dependence compared to the diaphragm resonance. Consequently these parasitics lead to an offset capacitance independent of applied bias and do not influence the accuracy of measurement of C_1. These parasitic components do potentially degrade the signal levels when these devices are used as ultrasonic transducers.

In order to further characterize the transducers, we performed admittance measurements as a function of frequency and ambient pressure. Figure 4 shows a wide-range admittance measurement under coarse vacuum (pressure $P < 0.03$ atm). We observe a moderately sharp resonance near 3.47 MHz that is present only with a DC bias applied. There is a corresponding dip in the phase at the same frequency. (The phase shift away from the

reference differs from the ideal value of 90 degrees because of the parasitic parallel components mentioned above).

Additional measurements (not shown) confirm that, as expected, the resonance peak is independent of the polarity of the DC bias voltage and that its magnitude is proportional to the square of the DC bias voltage. Consequently the observed resonance can be unambiguously attributed to the diaphragm resonance despite the complications introduced by parasitic elements.

We have performed detailed measurements as a function of ambient pressure that show a number of interesting features. Figure 5 shows the results obtained at four different pressures ranging from coarse vacuum to atmospheric pressure. As expected, the resonance peak becomes stronger and narrower as the pressure is decreased. There is also a small but consistent shift of the resonant frequency to higher values as the pressure is increased. This occurs because air beneath the membrane contributes some small additional opposing force giving rise to an increase in the spring constant with ambient pressure. Finally, we note the appearance of fine structure at the lowest pressure. This fine structure is exactly repeatable and is not due to instrument noise or other defects of the measurement system. We believe that the fine structure is a consequence of varying resonant frequencies of the individual diaphragms resulting from slight differences in boundary conditions; for example, diaphragms along the edges of a transducer have support conditions different from those of diaphragms at the center of a transducer. In any event, the observed variation in resonant frequencies is only ±0.6%, indicating that these effects are small and that the diaphragms are very nearly identical.

Fitting the resonance curves in Fig. 5 to the functional form of eq. (7) yields values for the resonant frequency ω_0 and the ratio ω_0/Q. At the higher air pressures, up to atmospheric, the fit to a single resonant frequency is excellent, as illustrated for example in Fig. 7. However, for the lowest air pressure (coarse vacuum) multiple resonators with closely spaced resonant frequencies must be used. Figure 7 illustrates that a close fit can be obtained in this case using five resonators. The resonant frequency ω_0 plotted for this case is the strongest of the individual resonators.

B. Coupled transducers

Prior work on MEMS transducers has used air or fluid coupling and as a result sealed transducers have generally been necessary. Here we explore the bonding of transducers directly to solids. This yields better coupling than is possible for coupling through air and a more permanent arrangement than is possible using fluid coupling. We also seek to avoid sealing the release holes on the front surface of the transducers, as this requires an additional process step.

We previously reported bonding of transducers using cyanoacrylate adhesive applied to the solid surface [13].

This was successful in an initial demonstration but some large voids were observed and the yield of operating transducers was poor. In this work, we have used Gelest Zipcone CG silicone coating for bonding the transducers. With this coating, only a few small voids were observed and eight out of nine transducers were operable.

Figure 8 shows 1 MHz *C(V)* measurements for two bonded transducers (similar characteristics were measured for three other transducers on the same chip). The two capacitance curves are offset for clarity. Important differences between these measurements and measurements on unbonded devices are (1) the presence of hysteresis and (2) a smaller total change in capacitance (the fitted curve for an unbonded transducer is shown in black for comparison).

We attribute the hysteresis to "flow" of the silicone coating when subjected to a stress. Similar hysteresis was observed for several transducers on the same chip, indicating that all were bonded in a similar manner. After bonding, eight of nine transducers were operational while the ninth was electrically shorted. It is not known whether that transducer was defective when fabricated or whether it became shorted during the bonding process. We believe that the release holes are small enough to prevent the silicone from entering the cavity beneath the diaphragm. Evidently the diaphragms used in this work are sufficiently robust for this sort of handling, although it is not possible to predict the durability of larger diaphragms.

There may be alternative materials or combinations of materials that are more convenient or that give higher yield of bonded detectors. This could be addressed in future studies and the electrical characterization approach reported here may be useful for rapid evaluation of new bonding materials.

V. Modeling-C_1, Resonant Frequency, and Damping

In this section we develop models for the voltage coefficient of capacitance, resonant frequency, and damping, and we apply these models to the coupled and uncoupled transducers. Our objective is to relate the parameters of the single degree of freedom model to the physical structure of the diaphragm. This work also permits us to draw conclusions about the boundary condition at the diaphragm edge.

A. Capacitance voltage coefficient C_1

We consider a circular elastic diaphragm of radius a subjected to uniform static pressure P, and we measure r radially from the center. The solution for the deflection $w(r)$ is well-known [14] and is stated as

$$w(r) = \frac{P\left(a^2 - r^2\right)\left(\frac{5+\nu}{1+\nu}a^2 - r^2\right)}{64D} \tag{8}$$

for the case of simple supports, and

$$w(r) = \frac{P\left(a^2 - r^2\right)^2}{64D} \tag{9}$$

for the case of rigid supports. The quantity D is termed the flexural rigidity of the diaphragm and is calculated as

$$D = \frac{Eh^3}{12(1-\nu^2)} \cdot \tag{10}$$

Relevant material properties for polysilicon are Young's modulus $E = 180 \times 10^9$ N/m^2, Poisson's ratio $\nu = 0.22$ [15], and diaphragm thickness $h = 2.0$ microns.

In a parallel plate capacitor a voltage V produces a pressure on the plates equal to

$$P = \frac{\varepsilon_0 V^2}{2\left(g - w(r)\right)^2} \approx \frac{\varepsilon_0 V^2}{2g^2} \cdot \tag{11}$$

If the diaphragm of radius a overlays a slightly smaller circular electrode of radius b, the C_1 coefficient for a group of 180 electrodes can be reasonably calculated as

$$C_1 = 180 \cdot 2\pi \cdot \frac{\varepsilon_0}{g^2} \int_0^b w(r) \cdot r \cdot dr \cdot \tag{12}$$

In this analysis the hexagonal diaphragm is modeled as a circular diaphragm with radius $a = 42.5$ microns, which is the inscribed radius, and the bottom electrode is modeled as a circle with radius $b = 34.1$ μm, which preserves the area of that electrode. The coefficient C_1 is predicted to be 1.72×10^{-18} F/V^2 for the simply supported case and 0.319×10^{-18} F/V^2 for the rigidly supported case.

B. Resonant frequency

The lowest resonant frequency of a hexagonal diaphragm of leg length L and thickness h is known [16] and is expressed as

$$f_0 = \frac{K}{2\pi L^2}\sqrt{\frac{D}{\rho h}} \tag{13}$$

where the mass density $\rho = 2300$ kg/m^3 and for our device $L = 49.1$ microns. The coefficient K depends on the boundary conditions at the edges; for a simply supported diaphragm $K = 7.152$ while for a rigidly supported diaphragm $K = 12.81$. As the actual boundary condition is intermediate between these two cases we expect

$$2.482 \text{ MHz} < f_0 < 4.444 \text{ MHz} \cdot \tag{14}$$

The measured resonant frequency of 3.47 MHz is between the two limits, as would be expected.

It is instructive to perform the same calculation for a circular diaphragm of radius a, using $a = 42.5$ microns which corresponds to the inscribed radius. For the circular diaphragm, $K = 4.858$ for the simply supported case

and 10.22 for the rigidly supported case. Accordingly, the range of resonant frequencies predicted by this equivalent circular diaphragm is

$$2.250\,\text{MHz} < f_0 < 4.733\,\text{MHz}. \tag{15}$$

Note that the frequency range predicted in Eq. 10 for the circular diaphragm with a = 42.5 microns is comparable to the frequency range predicted in Eq. 9 for the hexagonal diaphragm with L = 49.1 microns,

The influence of the residual film stress can be evaluated by comparing it to the in-plane critical (buckling) stress for a simply supported circular diaphragm. The critical stress is denoted σ_{cr} and is calculated from [14]

$$\sigma_{cr} = \frac{4.2D}{a^2 h} \tag{16}$$

For the circular diaphragm with a = 42.5 microns, σ_{cr} is found to be -150 MPa. Because the residual film stress of –10 MPa is small in comparison to σ_{cr}, the presence of the residual film stress is shown in the literature [14] to have minimal influence on the diaphragm stiffness and the resonant frequency.

C. Damping

In order to estimate parameters for a single degree of freedom (SDOF) dynamic model, we replace the hexagonal diaphragm with a simply supported circular diaphragm having the same resonant frequency. (An alternate approach would have been to fix the radius at 42.5 microns and to model the diaphragm with a support condition intermediate between simply supported and fixed. However, it would be quite cumbersome to model such an intermediate support condition, and the clarity of the approach would be lost. For that reason, we consider it more instructive to examine a simply supported circular diaphragm having the same resonant frequency.) The lowest mode shape for a simply supported circular diaphragm, normalized to a unit displacement at the center of the diaphragm, is $W(r)$ and is obtained from the literature [14] as

$$W(r) = 1.043 J_0(\kappa r) - 0.0427 I_0(\kappa r) \tag{17}$$

where κr is a nondimensional radial coordinate, $\kappa = 2.204/a$, and J_0 and I_0 are Bessel functions.

Matching the resonant frequency of 3.47 MHz requires that radius a = 34.3 microns, at which we find the equivalent SDOF mass m^* and SDOF spring constant k^* as follows

$$m^* = 2\pi\rho h \int_0^a W^2(r) r dr = 0.2866\,\pi a^2 \rho h = 4.87 \times 10^{-12}\ kg \tag{18}$$

and

$$k^* = 2\pi \frac{1}{D}\int_0^a r\left(\left[W''(r)+\frac{1}{r}W'(r)\right]^2 - 2\frac{1-\nu}{r}W'(r)W''(r)\right)dr \qquad (19)$$
$$= 2.33\times 10^3 \ N/m$$

Calculating $\omega_0 = (k^*/m^*)^{1/2}$ and dividing by 2π yields the resonant frequency of 3.47 MHz. We note that the equivalent SDOF mass m^* is 28.66% of the gross mass, and similarly that the equivalent SDOF area S^* is 28.66% of the gross area, or 1.06×10^{-9} m^2 for a single diaphragm.

So far the influence of air on the resonant frequency and damping has been neglected. The distributed stiffness contributed by a pressure change of the air trapped beneath the diaphragm, envisioned as a spring stiffness per unit area, is obtained from Boyle's law as simply p_{air}/g, where p_{air} is the air pressure in N/m^2 and g is the gap dimension in m. This distributed stiffness is converted into an equivalent additional SDOF spring constant k^*_{air} by multiplying p_{air}/g by the square of the mode shape and integrating over the area, or equivalently by multiplying pair/g by the equivalent SDOF area S^*, to obtain

$$k^*_{air} = 2\pi p_{air}\frac{1}{g}\int_0^a W^2(r)rdr = 5.30\times 10^{-4}\, p_{air} \qquad (20)$$

The additional SDOF spring constant k^*_{air} is added to the SDOF spring constant of the diaphragm to predict a shift in resonant frequency from ω_0 as follows

$$\frac{\omega}{\omega_0} = \sqrt{\frac{k^* + k^*_{air}}{k^*}} \ . \qquad (21)$$

At atmospheric pressure (taking p_{air} as 10^5 N/m^2) ω/ω_0 is calculated to be 1.011, whereas ω/ω_0 was observed to be 1.0046. Because the air is not completely trapped beneath the diaphragm, some air can escape from the etch holes and therefore an observed shift smaller than that calculated in (21) is reasonable.

The radiation of ultrasonic energy provides one contribution to damping. As noted earlier, radiation of acoustic energy across the equivalent SDOF area S^* yields a Q factor given by

$$Q_{radiation} = \frac{\sqrt{m^* k^*}}{Z_{air} S^*} = 233 \qquad (22)$$

where Z_{air} is 430 N-s/m^2 and where we have used m^*, k^*, and S^* from the single-degree-of-freedom model.

Damping is also present in the form of squeeze-film damping, an instance of lubrication theory [17]. Consider two planar surfaces separated by a gap g with velocity of normal approach $\dot{g}$, causing flow of the fluid within that gap. For an incompressible fluid with dynamic viscosity μ, the fluid pressure p is governed by the Reynolds equation (in polar coordinates)

$$\frac{1}{r}\frac{\partial}{\partial r}\left(r\frac{\partial p}{\partial r}\right)+\frac{1}{r^2}\frac{\partial^2 p}{\partial \theta^2}=\frac{12\mu\dot{g}}{g^3} \tag{23}$$

where the air viscosity $\mu = 18 \times 10^{-6}$ Pa-s at atmospheric pressure. Eq. 23 shows that the fluid pressure is inversely proportional to g^3, causing the pressure to become large when the film thickness is small, and proportional to $\dot{g}$, causing the pressure to act as an equivalent viscous damping effect.

In our diaphragm, the fluid flow is the movement of air through the etch holes. Each etch hole is 5 microns square and is spaced on a square 30-micron grid. Whereas an exact analysis would require a multi-physics finite element model, an approximation is suggested here to be used in our analysis of the SDOF case. We replace each grid square with a circular piston traveling within a cylinder, having outer radius b_o = 16.9 microns and a central circular vent hole of inner radius b_i = 2.82 microns, preserving the area in one grid square. The symmetry of the circular piston simplifies the governing Reynold's equation to

$$\frac{1}{r}\frac{\partial}{\partial r}\left(r\frac{\partial p}{\partial r}\right)=\frac{12\mu\dot{g}}{g^3} \tag{24}$$

A solution for p(r) is found by double integration, with appropriate boundary conditions that $p(b_i) = 0$ and that $\frac{\partial p}{\partial r}(b_o) = 0$. The force F acting against the face of the piston is then calculated as

$$F = 2\pi\int_{b_i}^{b_o} prdr = 3.65\times10^{-6}\,\dot{g} \tag{25}$$

This result describes an equivalent viscous damper with dashpot constant $c = 3.65\text{x}10^{-6}$ N-s/m.

In our model we consider the five etch holes nearest the center to represent the location of discrete dashpots, that are transformed into one equivalent SDOF dashpot by summing the product of each dashpot constant by the square of the mode shape at each etch hole location. In our geometry the equivalent SDOF dashpot constant is $\boxed{c^*} = 4.15 \times 10^{-6}$ N-s/m. (The one vent hole at the center, where the mode shape amplitude is 1.0, is the dominant contribution to the equivalent dashpot constant, because the diaphragm velocity at the four next nearest dashpots, each 30 microns away from the center, is very low.) The Q factor associated with the squeeze film damping effect for the single degree of freedom system is then obtained as

$$Q_{squeeze\ film} = \omega_0 \cdot \frac{m^*}{c^*} = 29.1 \tag{26}$$

leading to a predicted combined Q value calculated as

$$Q = \frac{1}{\frac{1}{Q_{radiation}}+\frac{1}{Q_{squeeze\ film}}} = 25.9 \tag{27}$$

Our calculation for squeeze film damping assumed incompressible flow, whereas the air in the gap is compressible, as already evidenced by the shift of resonant frequency with pressure. For a given transverse velocity of the piston the fluid velocity, and the viscosity stresses, will be lower in the case of compressible flow. Therefore, the dashpot constant obtained above overestimates the actual squeeze film damping, which must be recognized when comparing the predicted Q of 25.9 to the Q of 49.6 that was observed at atmospheric pressure. As expected, the observed Q increases as the air pressure is decreased, and we attribute the value observed at vacuum (Q = 910) to internal friction in the polysilicon itself and other unavoidable loss mechanisms.

Finally, we consider the losses in coupled transducers. Squeeze film damping should be absent in devices with completely covered holes. The acoustic impedance of the silicone coating used here has an acoustic impedance measured as $Z_{medium} = 1.7 \times 10^6$ kg/m^{2}s, approximately a factor of 3700 larger than the impedance of air. Consequently the Q of bonded transducers is predicted to be very small and no resonant behavior is expected. In measurements of bonded transducers (not shown) no resonance is in fact observed.

These results also provide insight into the performance of diaphragm transducers with open etch holes that are operated in air. In such transducers losses due to squeeze film damping can have either beneficial or detrimental effects. Damping has the effect of reducing the transducer Q and thus increasing the bandwidth, which is generally desirable. However, the additional damping also leads to inefficient conversion of electrical energy to ultrasonic energy. The expressions developed above can be used to predict these effects in tranducers with different geometry.

Finally, the low Q of bonded transducers should not be regarded as an undesirable characteristic. Physically, a low Q means that the diaphragm is strongly coupled to the bonding medium and that it will closely follow any motion of the medium. As a result, coupled diaphragms are highly suitable for use as detectors of ultrasonic waves. In an accompanying paper we will illustrate successful operation of these detectors over a wide frequency range and their application to phased-array sensing.

VI. Conclusions

Polysilicon diaphragms for application as ultrasonic transducers have been fabricated and electrically characterized. Unbonded diaphragms have been measured at atmospheric pressure and also at reduced pressure. These diaphragms exhibit high quality factors ranging from 50 (in air) to 910 (in vacuum). The capacitance change with applied DC bias is well predicted by a model assuming simply supported diaphragm boundaries, while the resonant frequency is intermediate between predictions for simply supported and rigidly supported models. Parameters for a single-degree-of-freedom model have been derived from the mode shape of a simply supported

diaphragm. Reasonable agreement with the measured quality factors and resonant frequency shift with pressure was obtained.

A particularly important aspect of this work is the study of diaphragms that are bonded to solid materials. These diaphragms are not damaged by the bonding process and show capacitance-voltage characteristics that are consistent with bonding to a deformable medium. Bonded diaphragms show no evidence of resonant behavior and consequently should be useful as wideband acoustic detectors.

ACKNOWLEDGMENTS

This work has been funded by the Commonwealth of Pennsylvania through the Pennsylvania Infrastructure Technology Alliance program, administered at Carnegie Mellon by the Institute for Complex Engineering Systems, and by gifts from Krautkramer Inc. The authors would also like to thank Kevin Fredrick for performing wirebonding.

REFERENCES

[1] P.-C. Eccardt, K. Niederer, T. Scheiter, and C. Hierold, "Surface micromachined ultrasound transducers in CMOS technology," *1996 IEEE Ultrasonics Symposium Proc.*, pp. 959-962 (1996).

[2] A.G. Bashford, D.W. Schindel, D.A. Hutchins, "Micromachined ultrasonic capacitance transducers for immersion applications," *IEEE Transactions on Ultrasonics, Ferroelectrics, and Frequency Control*, vol. 45, pp. 367-375 (1998).

[3] X. Jin, I. Ladabaum, F.L. Degertekin, S. Calmes, and B.T. Khuri-Yakub, "Characterization of one-dimensional capacitive micromachined ultrasonic immersion transducer arrays," *IEEE Journal of Microelectromechanical Systems*, vol. 8, pp. 100-114 (1999).

[4] X. Jin, O. Oralkan, F.L. Degertekin, and B.T. Khuri-Yakub, "Characterization of one-dimensional capacitive micromachined ultrasonic immersion transducer arrays," *IEEE Transactions on Ultrasonics, Ferroelectrics, and Frequency Control*, vol. 48, pp. 750-760 (2001).

[5] O. Oralkan, X.C. Jin, K. Kaviani, A.S. Ergun, F.L.Degertekin, M. Karaman, and B.T. Khuri-Yakub, "Initial pulse-echo imaging results with one-dimensional capacitive micromachiined ultrasonic transducer arrays," *2000 IEEE Ultrasonics Symposium Proc.*, pp. 959-962 (2000).

[6] P.-C. Eccardt, K. Niederer, and B. Fischer, "Micromachined transducers for ultrasound applications," *1997 IEEE Ultrasonics Symposium Proc.*, pp. 1609-1618 (1997).

[7] S.T. Hansen, B.J. Mossawir, A.S. Ergun, F. L. Degertekin, and B.T. Khuri-Yakub, "Air-coupled nondestructive evaluation using micromachined ultrasonic transducers," *1999 IEEE Ultrasonics Symposium Proc.*, pp. 1037-1040 (1999).

[8] A. Jain, I.J. Oppenheim, and D.W. Greve, in preparation.

[9] I. Ladabaum, X. Jin, S.T. Soh, A. Atalar, and B.T. Khuri-Yakub, "Surface Micromachined Capacitive Ultrasonic Transducers," IEEE Trans. Ultrasonics, Ferroelectrics, and Frequency Control, vol. 45, pp. 678-690, May 1998.

[10] Fundamentals of Ultrasonics, J. Blitz, p. 53 (Butterworths, London, 1963).

[11] Details of the MUMPS process are available from JDS Uniphase, MEMS Business Unit (Cronos), 3026 Cornwallis Road, Research Triangle Park, NC 27709 and also at http://www.memsrus.com/mumps.pdf.

[12] Gelest, Inc., 11 East Steel Road, Morrisville, PA 19067.

[13] A. Jain, D.W. Greve, , and I.J. Oppenheim, "A MEMS Ultrasonic Transducer for Monitoring of Steel Structures," *Proceedings of SPIE Vol. 4696, Smart Structures and Materials -- Smart Systems for Bridges, Structures, and Highways*, Paper 4696-31, San Diego, March 2002.

[14] S. P. Timoshenko and S. Woinowsky-Krieger, Theory of plates and shells, 2nd edition, New York: McGraw Hill, 1959.

[15] W.N. Sharpe, B. Yuan, and R. Vaidyanathan, "Measurements of Young's Modulus, Poisson's ratio, and Tensile Strength of Polysilicon," *Proceedings of The Tenth Annual International Workshop on Micro Electro Mechanical Systems. An Investigation of Micro Structures, Sensors, Actuators, Machines and Robots*, pp. 424-9 (IEEE, New York, NY, USA (1997).

[16] A. W. Leissa, *Vibration of plates*, Washington, D.C.: NASA SP-160, 1969.

[17] *CRC Handbook of Lubrication*, E. Richard Booser, ed., *CRC Handbook of Lubrication, Vol. II, Theory and Design*, CRC Press, Boca Raton, 1983.

FIGURE CAPTIONS

Fig. 1. Ultrasonic transducers investigated in this study: (left) detail sketch of a single diaphragm unit; and (right) a single transducer consisting of 180 parallel diaphragms.

Fig. 2. Fabrication process flow for the MEMS ultrasonic transducer. The two plates of the transducer are formed from the POLY0 and POLY1 layers.

Fig. 3. 1 MHz C(V) characteristic for a transducer: (□) measured data and (—) fit to eq. (3).

Fig. 4. Measured admittance $|Y(\omega)|$ for diaphragm: (black) $V_{DC} = 0$ V and (gray) $V_{DC} = 30$ V. Insets: (upper left) detail of $|Y(\omega)|$ and (lower right) detail of phase in degrees.

Fig. 5. Measured admittance magnitude $|Y(\omega)|$ as a function of pressure: (○) coarse vacuum; (□) 0.29 atm; (◇) 0.61 atm; (+) 1 atm (all with $V_{DC} = 35$ V) and (—) coarse vacuum, $V_{DC} = 0$ V.

Fig. 6. Admittance data (○) and fit (—): (top) 0.29 atm and (bottom) coarse vacuum.

Fig. 7. Extracted resonance parameters from data (---, □) resonant frequency and (—, □) damping parameter ω_0/Q.

Fig. 8. Measured 1 MHz C(V) data for two bonded transducers: (□,□) increasing bias and (○,○) decreasing bias. The capacitance zero has been offset for better visibility. The dotted curve shows the capacitance variation for an unbonded transducer for comparison.

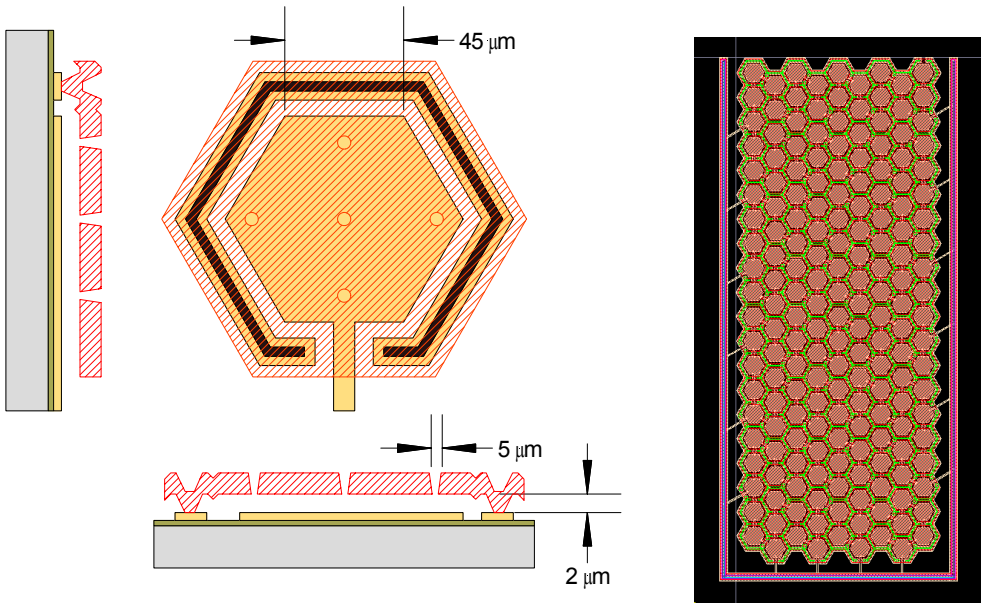

Fig. 1. Ultrasonic transducers investigated in this study: (left) detail sketch of a single diaphragm unit; and (right) a single transducer consisting of 180 parallel diaphragms.

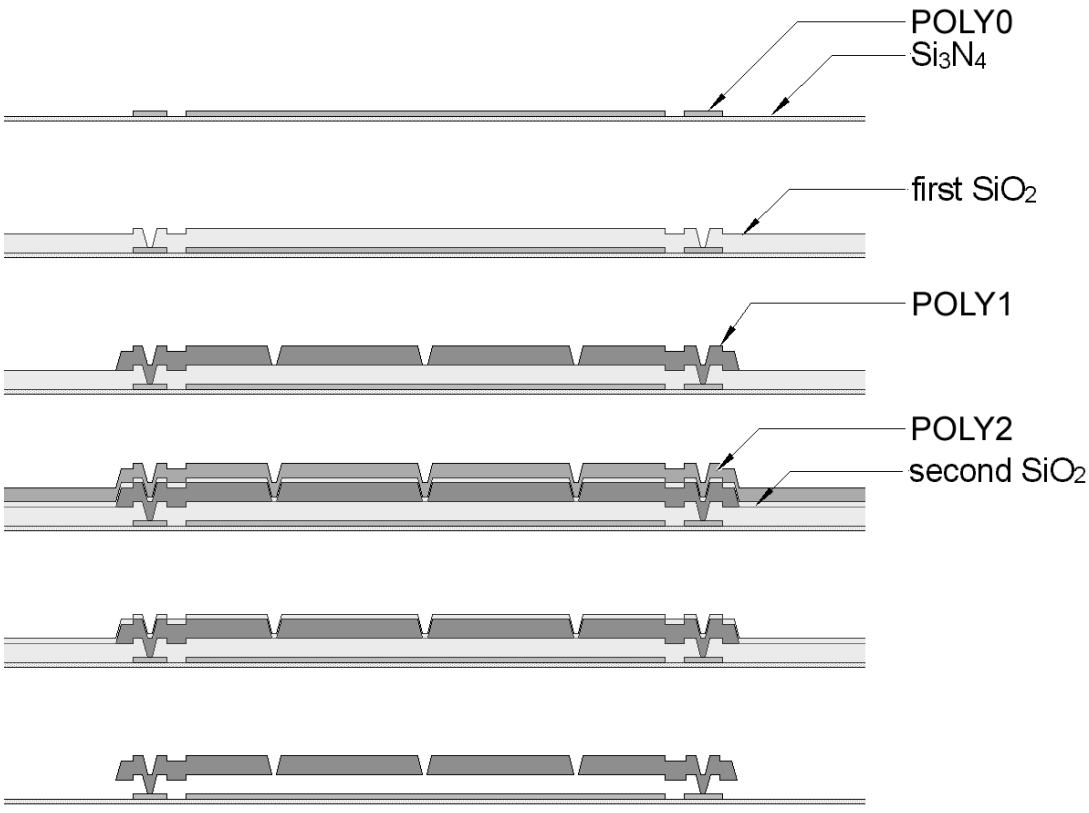

Fig. 2. Fabrication process flow for the MEMS ultrasonic transducer. The two plates of the transducer are formed from the POLY0 and POLY1 layers.

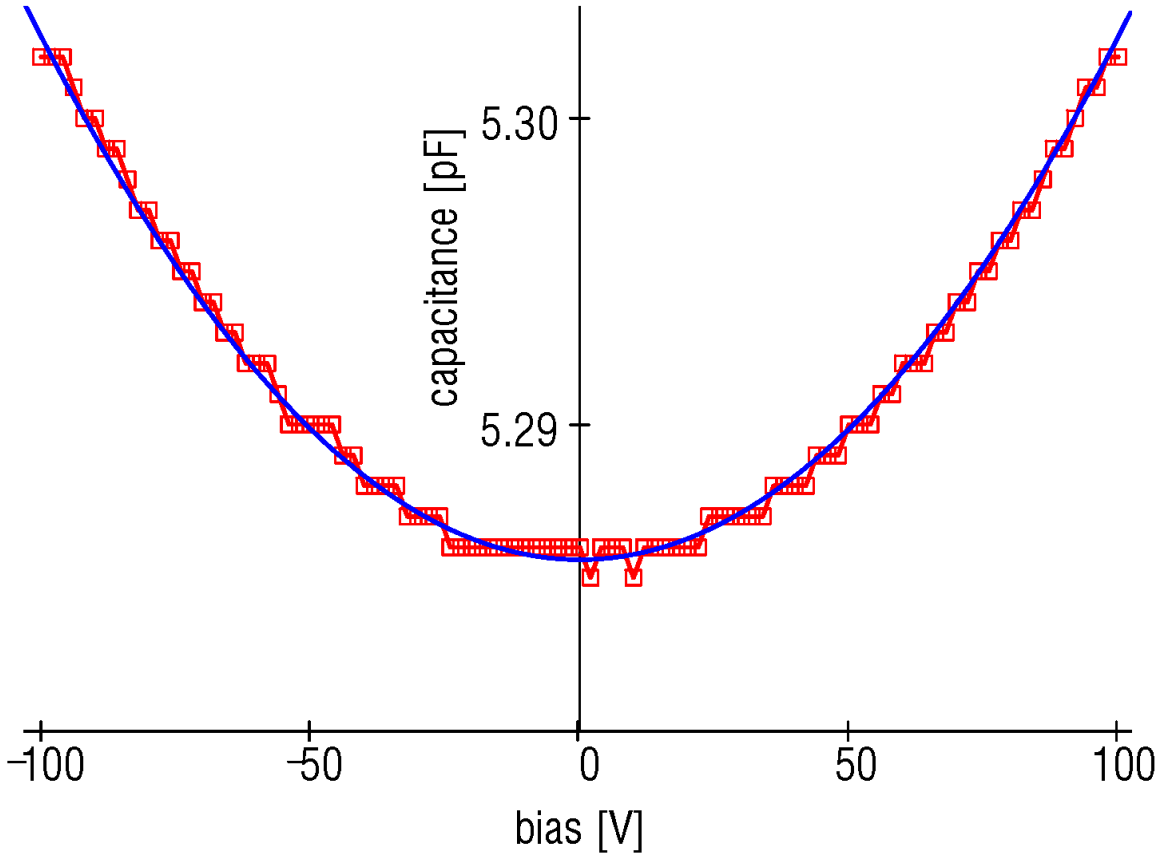

Fig. 3. 1 MHz C(V) characteristic for a transducer: (□) measured data and (—) fit to eq. (3).

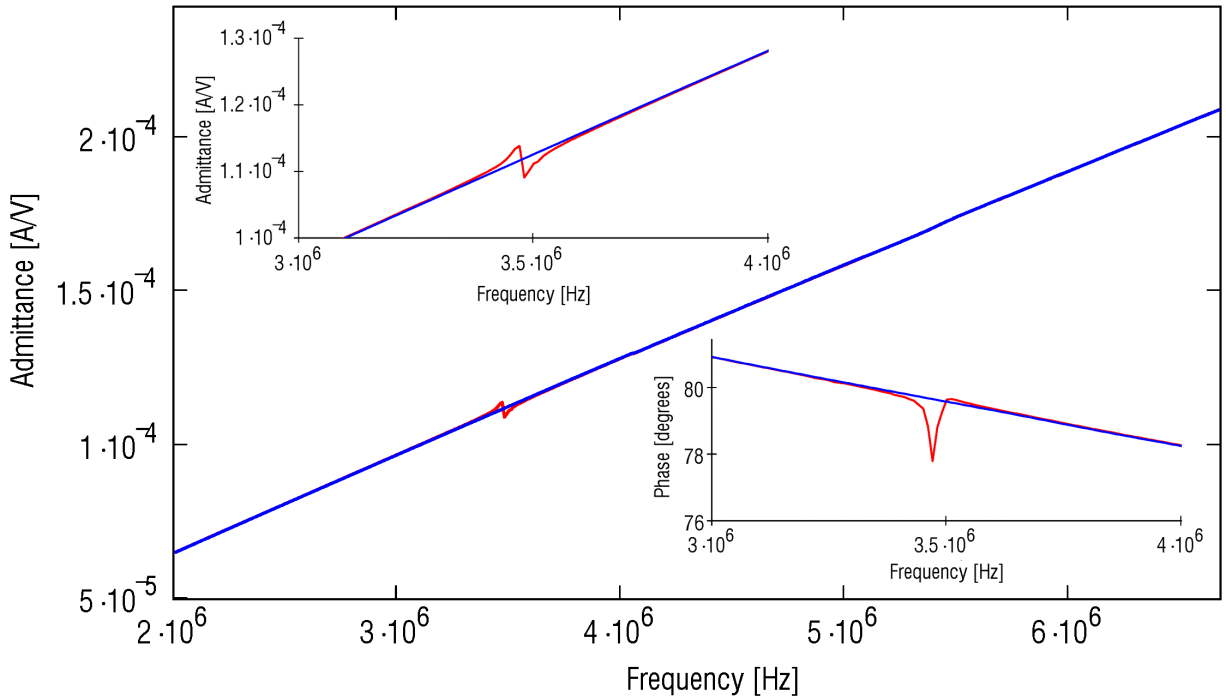

Fig. 4. Measured admittance $|Y(\omega)|$ for diaphragm: (black) $V_{DC} = 0$ V and (gray) $V_{DC} = 30$ V. Insets: (upper left) detail of $|Y(\omega)|$ and (lower right) detail of phase in degrees.

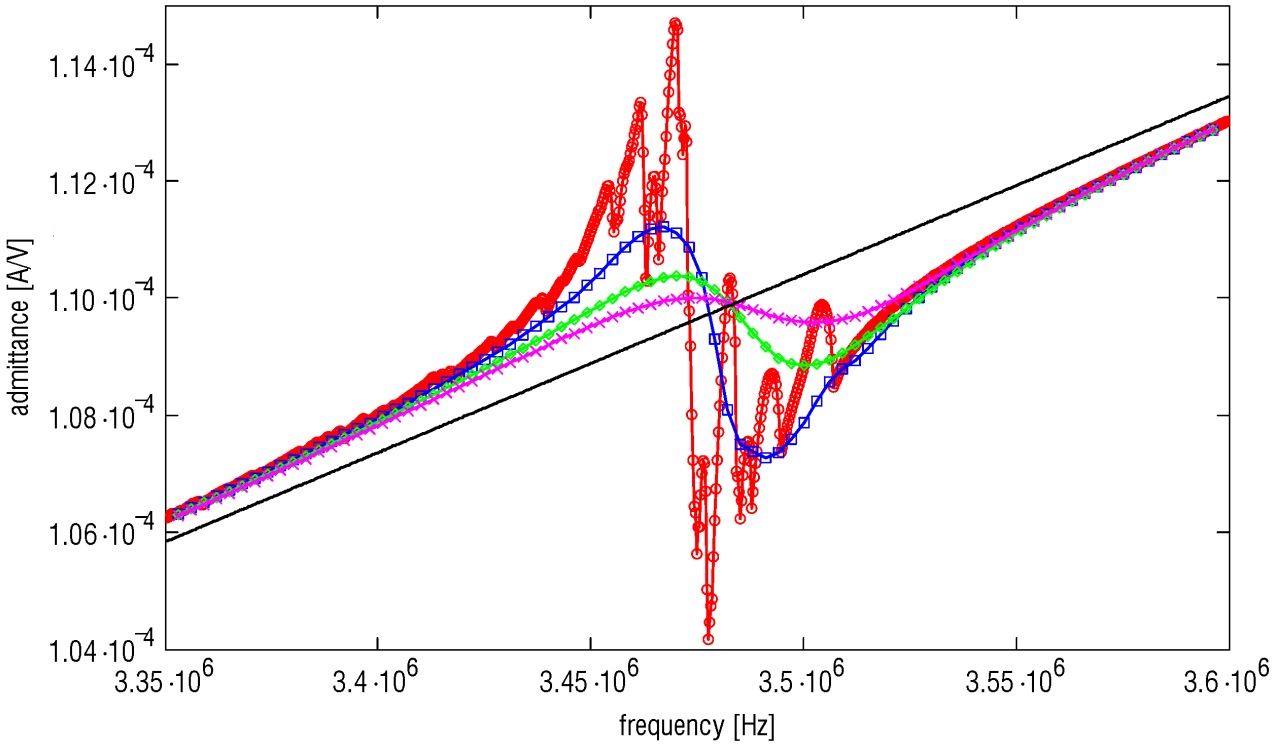

Fig. 5. Measured admittance magnitude $|Y(\omega)|$ as a function of pressure: (○) coarse vacuum; (□) 0.29 atm; (◇) 0.61 atm; (+) 1 atm (all with $V_{DC} = 35$ V) and (—) coarse vacuum, $V_{DC} = 0$ V.

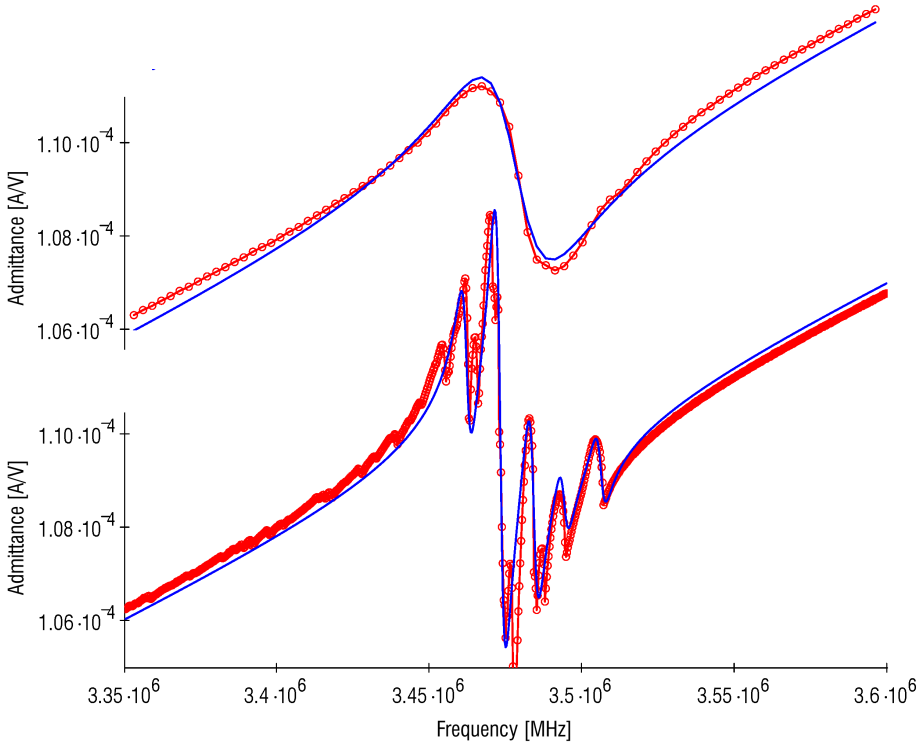

Fig. 6. Admittance data (O) and fit (—): (top) 0.29 atm and (bottom) coarse vacuum.

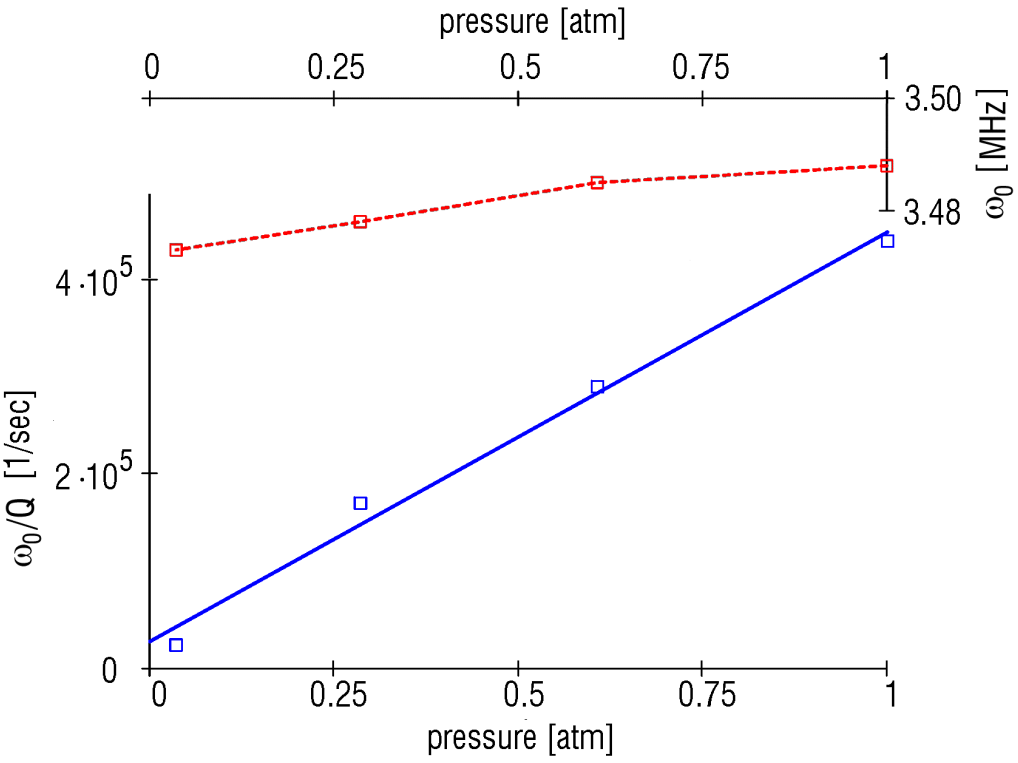

Fig. 7. Extracted resonance parameters from data (---, □) resonant frequency and (—, □) damping parameter ω_0/Q.

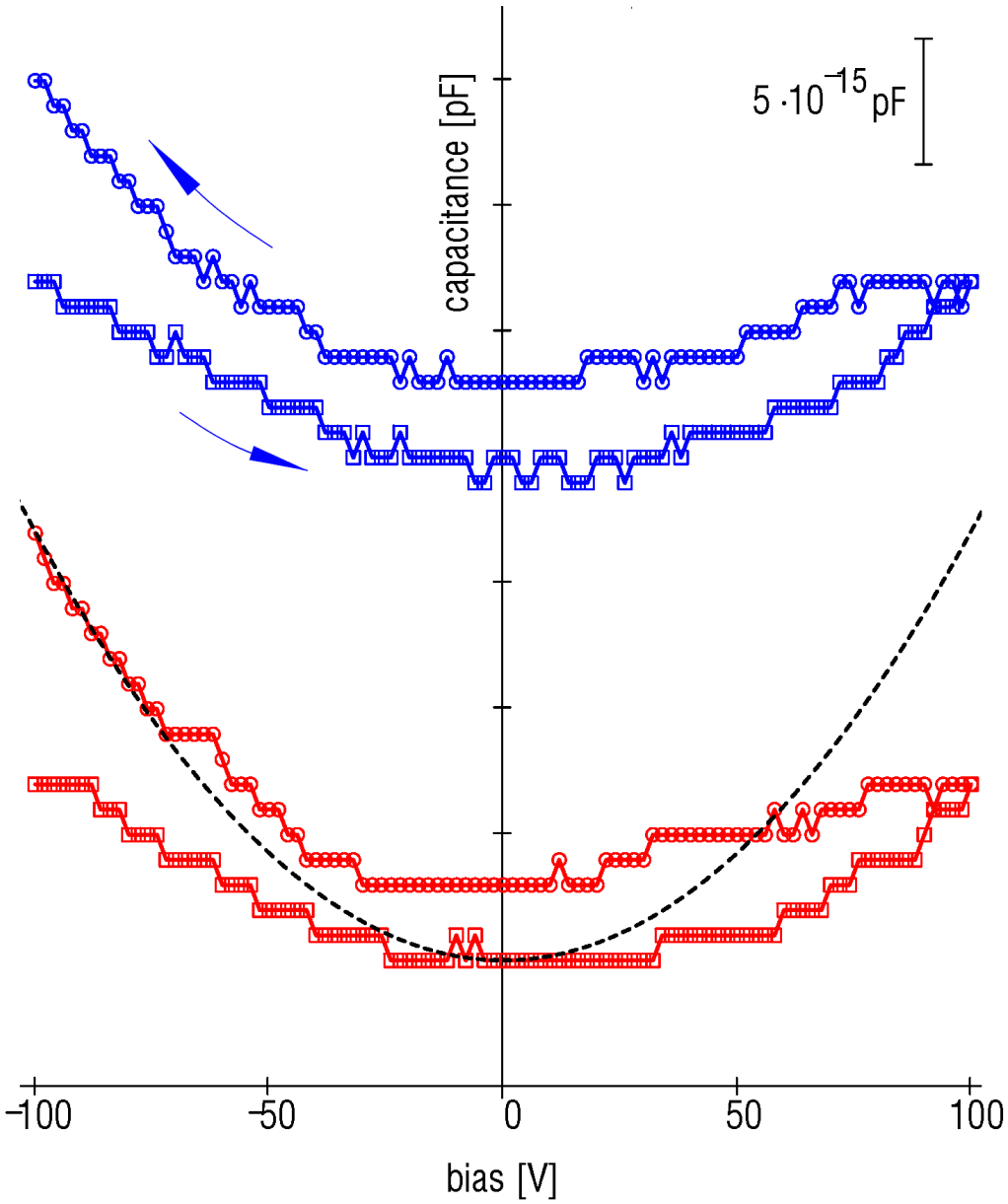

Fig. 8. Measured 1 MHz C(V) data for two bonded transducers: (□,□) increasing bias and (○,○) decreasing bias. The capacitance zero has been offset for better visibility. The dotted curve shows the capacitance variation for an unbonded transducer for comparison.